

## Dynamics and Structure of Mesoscale Error Covariance of a Winter Cyclone Estimated through Short-Range Ensemble Forecasts

FUQING ZHANG

*Department of Atmospheric Sciences, Texas A&M University, College Station, Texas*

(Manuscript received 14 April 2004, in final form 10 February 2005)

### ABSTRACT

Several sets of short-range mesoscale ensemble forecasts generated with different types of initial perturbations are used in this study to investigate the dynamics and structure of mesoscale error covariance in an intensive extratropical cyclogenesis event that occurred on 24–25 January 2000. Consistent with past predictability studies of this event, it is demonstrated that the characteristics and structure of the error growth are determined by the underlying balanced dynamics and the attendant moist convection. The initially uncorrelated errors can grow from small-scale, largely unbalanced perturbations to large-scale, quasi-balanced structured disturbances within 12–24 h. Maximum error growth occurred in the vicinity of upper-level and surface zones with the strongest potential vorticity (PV) gradient over the area of active moist convection. The structure of mesoscale error covariance estimated from these short-term ensemble forecasts is subsequently flow dependent and highly anisotropic, which is also ultimately determined by the underlying governing dynamics and associated error growth. Significant spatial and cross covariance (correlation) exists between different state variables with a horizontal distance as large as 1000 km and across all vertical layers. Qualitatively similar error covariance structure is estimated from different ensemble forecasts initialized with different perturbations.

### 1. Introduction

Immediately following the poorly forecasted, intense snowstorm of 24–25 January 2000, extensive studies were conducted to explore the possible reasons for the forecast failure at different temporal and spatial scales (e.g., Tracton and Du 2001; Buizza and Chessa 2002; Langland et al. 2002; Zhang et al. 2002, hereafter ZSR02; Zupanski et al. 2002; Jang et al. 2003). All of these studies concluded that errors in the initial conditions might have contributed significantly to the real-time forecast difficulty. More recently, Zhang et al. (2003, hereafter ZSR03) demonstrated that the mesoscale predictability can be seriously limited by strong upscale growth of small-scale small-amplitude initial error in the presence of moist convection, much as foreseen by Lorenz (1969). Consistent with this result, Buizza and Chessa (2002) pointed out the significance of including stochastic perturbations in the global en-

semble prediction system at the European Centre for Medium-Range Weather Forecasts (ECMWF). The inherent rapid growth of forecast error from convective scales and from stochastic processes suggests the need for short-range mesoscale probabilistic forecasts through ensembles. However, since uncertainties in the initial analysis in practice remain large, significant prediction skill can be gained with better data assimilation techniques (Zupanski et al. 2002; Jang et al. 2003).

One of the key issues for data assimilation is the specification of background error covariance. Although the deficiencies of isotropic and stationary representations of background error covariance have long been realized in the literature (e.g., Benjamin and Seaman 1985; Cohn and Parrish 1991; Daley 1992; Evensen 1994; Cohn 1997; Talagrand 1997), an isotropic and stationary error correlation is commonly used for data assimilation at most operational centers, such as the National Centers for Environmental Prediction (NCEP; Bishop et al. 2001). Over the past decade, ensemble forecasting has emerged as a powerful tool for numerical weather prediction (Tracton and Kalnay 1993; Molteni et al. 1996; Toth and Kalnay 1997). Ensemble forecasting not only has the promise of producing the mini-

---

*Corresponding author address:* Dr. Fuqing Zhang, Department of Atmospheric Sciences, Texas A&M University, 3150 TAMU, College Station, TX 77843-3150.  
E-mail: fzhang@tamu.edu

mum-error estimate of the future atmospheric state, it also provides uncertainties associated with this estimate and thus provides information valuable for estimating the flow-dependent background error covariance (Evensen 1994).

The ensemble-based data assimilation method (ensemble Kalman filter or EnKF; Evensen 1994), which uses short-term ensemble forecasts to estimate flow-dependent background error covariance, has recently been implemented in various atmospheric and oceanic models. These models vary from idealized examples based on simplified equation sets to those based on the complete, primitive equations with assimilation of real observations (Houtekamer and Mitchell 1998; Hamill and Snyder 2000; Keppenne, 2000; Keppenne and Rienecker 2002; Zhang and Anderson 2003; Snyder and Zhang 2003; Houtekamer et al. 2005; Whitaker et al. 2004; Dowell et al. 2004). These experimental studies demonstrated the feasibility and effectiveness of the EnKF for different scales and flows of interest and the advantages of using the EnKF over existing data assimilation schemes, which assume stationary, isotropic background error covariance.

With exceptions such as Hamill (2005, his Figs. 6–8), few studies have examined the detailed structure and the degree of anisotropy of background error covariance estimated from the ensemble forecast. Even less studied is the error growth dynamics that leads to the flow-dependent error covariance structure for regional or mesoscale atmospheric flows. In this study, several sets of mesoscale ensemble forecasts initialized with different perturbation generation methods are used to investigate the dynamics and structure of mesoscale error covariance in the context of an explosive extratropical cyclogenesis event. The model and experimental design will be described in section 2. Section 3 examines forecast uncertainties and error growth dynamics derived from different sets of short-term mesoscale ensemble forecasts. Demonstrations of the flow-dependent mesoscale error covariance are presented in section 4. Section 5 contains the concluding remarks.

## 2. Experimental design

### a. Forecast model

The study uses the fifth-generation Pennsylvania State University–National Center for Atmospheric Research (PSU–NCAR) Mesoscale Model (MM5; Dudhia 1993). The model has 27 vertical layers with the model top at 100 hPa. The horizontal domain covers the continental United States with a grid spacing of 30 km (Fig. 1), the same as the coarse domain used in ZSR02 and ZSR03. The reference initial analyses at 1200 UTC 23

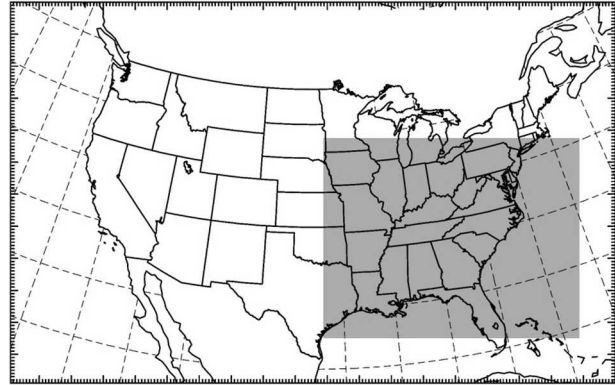


FIG. 1. Map of model domain. The region that is the focus of this study is indicated by the shaded area.

January and 0000 UTC 24 January 2000 are both generated using the real-time operational Eta Model analysis (Mesinger 1998) as the first guess and are then re-analyzed with conventional observations using the standard objective analysis tools available in MM5. Details and references on the model configurations and generation of the initial and boundary conditions can be found in ZSR02.

### b. Ensemble initializations

#### 1) RESCALED RANDOM PERTURBATIONS (EF-BGV)

First, “gridpoint” random perturbations with standard deviations of  $3 \text{ m s}^{-1}$  and  $3 \text{ K}$  are added to the reference analyses of the horizontal wind ( $U$  and  $V$ ) and temperature ( $T$ ) fields at all model grid points at 1200 UTC 23 January to generate five sets of perturbed initial conditions. Each of these initial states is then integrated with MM5 for 12 h. Since these initial perturbations are totally uncorrelated white noise, the domain-integrated difference total energy (DTE),

$$\text{DTE} = 0.5(U'U' + V'V' + kT'T'), \quad (1)$$

where primes denote difference between any two simulations and  $k = C_p/\text{Tr}$  ( $C_p = 1005.7 \text{ J kg}^{-1} \text{ K}^{-1}$  and the reference temperature  $\text{Tr} = 270 \text{ K}$ ), has decreased to  $\sim 20\%$  of its original value after 12 h. The decrease of DTE comes largely from numerical diffusion used in the forecast model, in which smaller-scale disturbances, especially those with scales smaller than the minimum resolvable wavelength (approximately 4–6 times the model grid spacing), are heavily damped. The decrease of DTE over these 12-h preforecast periods may also come from the geostrophic adjustment process because the initial gridpoint perturbations are largely unbalanced (Errico and Baumhefner 1987). Note that the isotropic initial perturbations do not decrease uni-

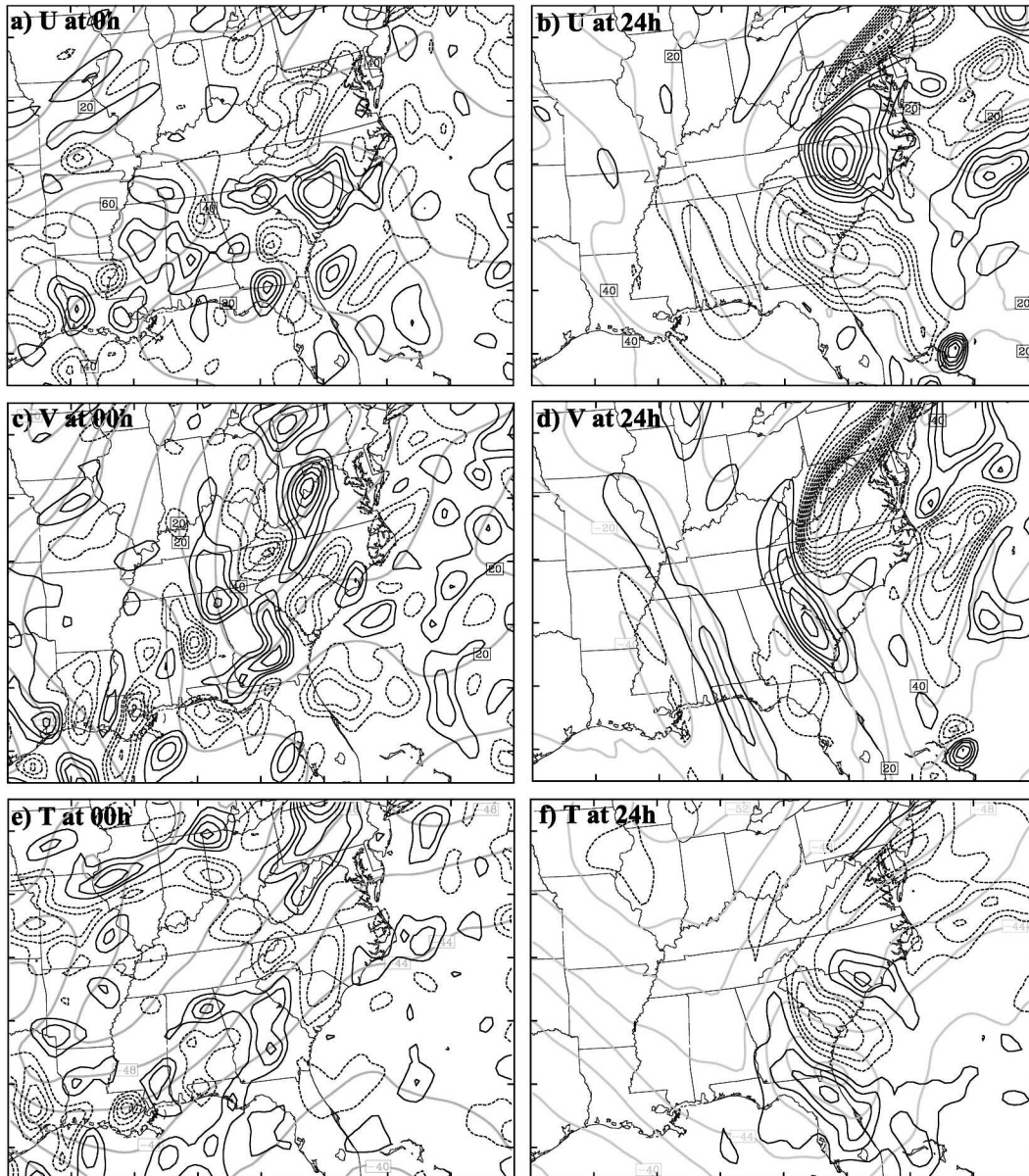


FIG. 2. The 300-hPa difference between member 1 and the mean of EF-BGV for (a)  $U$ , (c)  $V$ , and (e)  $T$  at 0 h, and for (b)  $U$ , (d)  $V$ , and (f)  $T$  at 24 h. Contour intervals for  $U$ ,  $V$ , and  $T$  are  $10 \text{ m s}^{-1}$  and  $2 \text{ K}$  for the ensemble mean (gray) and  $0.5 \text{ m s}^{-1}$  and  $0.5 \text{ K}$  for the difference (solid: positive; dashed: negative), respectively. Zero contours are suppressed in this and all subsequent figures.

formly across the model domain. Coherent difference structures, albeit still at relatively small scales, begin to develop from these random perturbations during the 12-h preforecast integration. The variations are maximized in the vicinity of the surface and upper-level fronts where strong gradients exist and over the region of moist activity. An example of such disturbances at the 300-hPa level after rescaling (described below) is shown in Figs. 2a,c,e.

The 12-h forecast difference of all prognostic vari-

ables between any of the two preforecast simulations is then rescaled according to the difference between the operational Eta analysis and ECMWF gridded analysis (in terms of domain-integrated DTE) valid at 0000 UTC 24 January (see ZSR02, p. 1623). That is to say, if the difference between two simulations after the 12-h preforecast is  $\text{DTE}_1$  and the difference between the Eta and ECMWF analyses is  $\text{DTE}_0$ , then the difference of all prognostic variables between these two simulations is rescaled by a factor of

$$\alpha = (\text{DTE}_0/\text{DTE}_1)^{1/2} \approx 2.0. \quad (2)$$

Thus, 10 sets of such rescaled differences (perturbations) are obtained from the five preforecast simulations. These perturbations are then added to (and subtracted from) the reference MM5 analysis valid at 0000 UTC 24 January to generate initial conditions for a 20-member ensemble forecast (“EF-BGV”). As a result, the reference MM5 analysis is the initial ensemble mean at this time. After the preforecast and rescaling, the initial DTE between the mean and each of the new ensemble members is equal to the DTE between the Eta and ECMWF analyses. The ensemble forecast generated with the rescaled perturbations thus has uncertainties comparable to those in real-time analysis-forecast systems (in terms of DTE). The ensemble generation method described herein is similar to the breeding method used at NCEP (Toth and Kalnay 1993) except that gridpoint random perturbations are used initially and the difference was scaled up instead of scaling down after the single 12-h breeding cycle. With only one breeding cycle, spectrum analyses show that initial uncertainties between ensemble members have more energy in smaller scales (and are thus less organized) than those between the Eta and ECMWF analysis. The error growth (ensemble spread) in the subsequent ensemble forecast is expected to be even greater when more organized and larger-scale initial uncertainties are used. The EF-BGV is initiated at 0000 UTC 24 January 2000 and integrated forward for 36 h. All ensemble members use the same real-time Eta forecast initialized at 0000 UTC 24 January as the lateral boundary conditions. The storm of interest and the analysis domain are chosen to be far away from the model inflow (west) boundary (Fig. 1) to minimize the impacts of using the same lateral boundary conditions in assessing the error growth dynamics and covariance (e.g., Vukicevic and Errico 1990).

Another set of ensemble forecasts (“EF-DRY”) is configured in exactly the same way as EF-BGV, except that the latent heating/cooling due to moist processes is turned off during the model integrations.

## 2) “BALANCED” RANDOM PERTURBATIONS (EF-BAL)

To test the sensitivity of the covariance structure, an independent set of ensemble forecasts (“EF-BAL”) is produced by randomly selecting initial perturbations from the *background error covariance* used by the MM5 three-dimensional variational data assimilation (DVAR) system developed at NCAR (Barker et al. 2004). The MM5 3DVAR analysis was performed on a transformed, geostrophically balanced streamfunction

field. Twenty such random perturbations of the streamfunction were thus created and then transformed to derive the balanced wind, temperature, and pressure perturbations (Barker et al. 2003, see 58–59), similar to the ensemble generation method used in Mitchell et al. (2002). These perturbations are then added to the reference MM5 analysis at 0000 UTC 24 January 2000 to generate a 20-member ensemble forecast integrated for 36 h with the same model configuration and boundary conditions as in EF-BGV.

## 3) GRIDPOINT RANDOM PERTURBATIONS (EF-RDM)

Another ensemble of 20 forecasts (“EF-RDM”) is produced by adding gridpoint random perturbations with standard deviations of  $3 \text{ m s}^{-1}$  and 3 K to the reference analyses of the horizontal wind ( $U$  and  $V$ ) and temperature ( $T$ ) fields at all model grid points at 0000 UTC 24 January 2004 and then integrating for 36 h with the same model configuration and boundary conditions as in EF-BGV. There are no correlations between perturbations of any two independent state vectors at the initial time. These perturbations are thus largely unbalanced with little projection to larger-scale flows.

## 3. The ensemble forecasts and error growth dynamics

Figure 3 shows the 24-h forecast of the mean sea level pressure (MSLP) and simulated radar reflectivity valid at 0000 UTC 25 January 2000 from three members of EF-BGV (Figs. 3a–c), EF-BAL (Figs. 3d–f), and EF-RDM (Figs. 3g–i). Despite a general agreement among the different forecasts with respect to the large-scale flow patterns, strong variability of all aspects of the snowstorm is found in the short-range ensemble forecasts between different sets of ensemble forecasts and between members in the same set of ensemble forecast using different initial conditions, consistent with the real-time, experimental NCEP short-range ensemble forecast of this event (Tracton and Du 2001). In real time, Raleigh, North Carolina, reported frozen precipitation starting at 0000 UTC 25 January followed by heavy snow in the next 12–18 h. Among all the members shown, we can see that 1) the central pressure of the surface cyclone varies from 991 to 997 hPa; 2) the structure and location of the surface cyclone centers differs significantly; and 3) most importantly, the locations of the instantaneous precipitation bands indicated by the simulated reflectivity can be completely shifted. For example, though the surface low pressure centers



FIG. 3. MSLP (every 2 hPa) and model-derived low-level averaged reflectivity (below 639 hPa, shaded) from three members of (a), (b), (c) EF-BGV, (d), (e), (f) EF-BAL, and (g), (h), (i) EF-RDM at the 24-h forecast time (0000 UTC 25 Jan 2000).

are very close to each other (Figs. 3b,c), most of the inland precipitation in Fig. 3b is along the coast of North Carolina, while most of the inland precipitation in Fig. 3c is along the coast of South Carolina and Georgia. As in Tracton and Du (2001), there are strong precipitation bands approaching the Washington, D.C., area in several of the ensemble members at the 36-h forecast time valid at 1200 UTC 25 January, which agrees well with real-time observations (not shown).

To compare the forecast sensitivity to the MM5 ini-

tial analysis in ZSR02 (their Fig. 15, p. 1629), the 36-h accumulated precipitation forecast difference between member 1 and the ensemble mean of EF-BGV is plotted in Fig. 4a. The precipitation evolution of all members of EF-BGV in a 240 km  $\times$  240 km rectangular box surrounding Raleigh is plotted in Fig. 4b. ZSR02 found that the maximum precipitation difference was as large as 40 mm over the Atlantic Ocean between experiments with and without the sounding from Little Rock, Arkansas, in the initial analysis (ZSR02, their Fig. 15a).

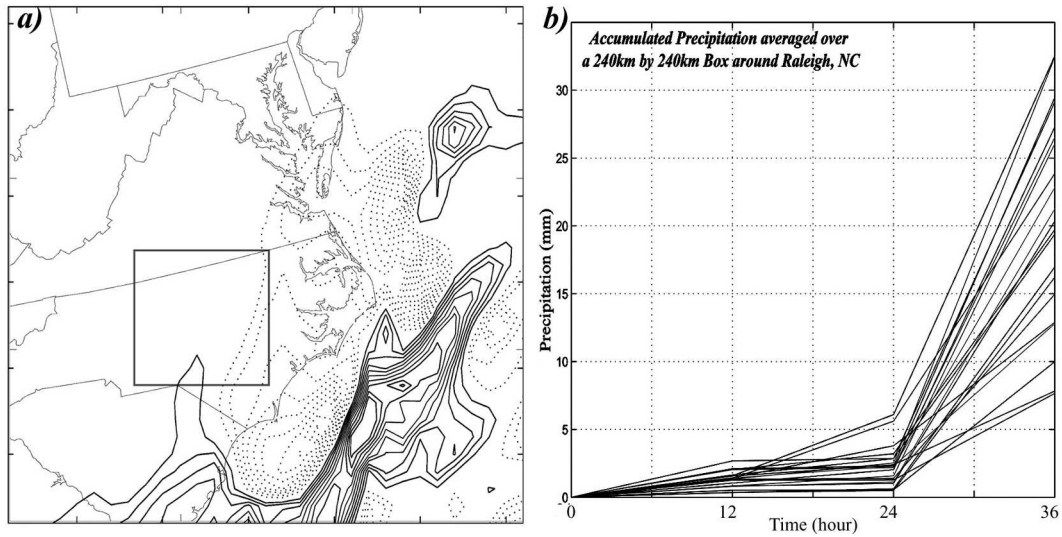


FIG. 4. (a) The 36-h accumulated precipitation difference ( $D = 10$  mm) between member 1 and the mean of EF-BGV. (b) Time evolution of the accumulated precipitation (mm) averaged over a  $240 \text{ km} \times 240 \text{ km}$  box around Raleigh, NC, for each member. The location of the box is shown in (a).

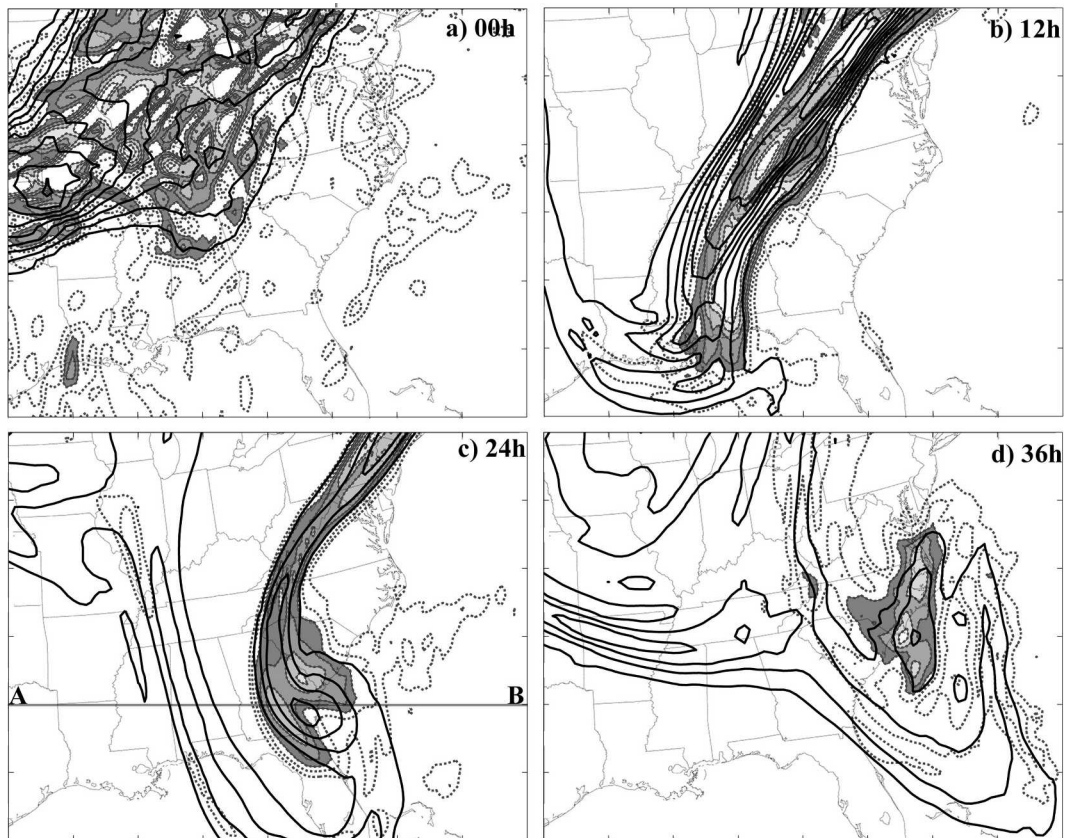


FIG. 5. Evolution of the 300-hPa mean PV (solid, every 1.0 PVU) and its std dev (dashed, every 0.25 PVU) starting from 0.5 PVU; greater than 1.0 PVU shaded) at the (a) 0-, (b) 12-, (c) 24-, and (d) 36-h simulation time.

They also found that the 36-h forecasted precipitation averaged over Raleigh can vary by 40% among the 10 individual sounding experiments (ZSR02, their Fig. 15b). In EF-BGV in which members have larger initial uncertainties, the maximum 36-h forecast precipitation difference is well over 100 mm (~4 in.) between member 1 and the ensemble mean (Fig. 4a). Moreover, the average 36-h precipitation forecast over Raleigh can differ by a factor of 4 (Fig. 4b). Large uncertainties of accumulated precipitation forecasts coincide with a high likelihood of moist convection, consistent with Mullen et al. (1999) and ZSR03 (their Fig. 6). Comparable variability of short-range precipitation forecasts were reported previously by Du et al. (1997) and Stensrud et al. (1999) with the NCEP short-range ensemble forecasting (SREF) system, although longer-term statistics of SREF displayed a general lack of error growth in mesoscale precipitation forecasts (Wandishin et al. 2001).

Consistent with large precipitation forecast uncertainty at 24 h (Fig. 3–4), the 300-hPa wind and temperature differences between the first member and the ensemble mean of EF-BGV at the 24-h forecast time (Figs. 2b,d,f) are also much larger, both in scale and in magnitude than the differences at the initial time (Figs. 2a,c,e). This suggests that the largely unbalanced, smaller-scale initial perturbations in EF-BGV evolved into quasi-balanced, larger-scale systematic differences over the 24-h forecast period. A similar transition also occurred in EF-RDM initialized with purely random perturbations (not shown). Figures 2–4 indicate that, by 24–36 h, all three ensemble experiments have developed a reasonable spread and therefore have been satisfactorily initialized. The upscale error growth in these ensemble forecasts is consistent with findings from various sensitivity experiments examined for this case in ZSR03. The scale change of growing errors for larger-scale flows has also been discussed previously (e.g., Farrell 1990; Buizza 1994; Barkmeijer et al. 1998; Tribbia and Baumhefner 2004).

The evolution of the balanced dynamics in the ensemble forecasts is further examined through the diagnosis of potential vorticity (PV). The evolution of the 300-hPa mean PV and its standard deviation (as a measure of spread) from EF-BGV are plotted in Fig. 5. Consistent with largely unbalanced wind and temperature perturbations from member 1 (Figs. 2a,c,e), large initial PV uncertainties at 300 hPa spread out all over the domain with incoherent structures (Fig. 5a). Nevertheless, after the short breeding cycle, there are numerous localized maxima along the strong gradients of the background (ensemble mean) PV, albeit still small in scale. After 12 h (Fig. 5b), the mean PV associated

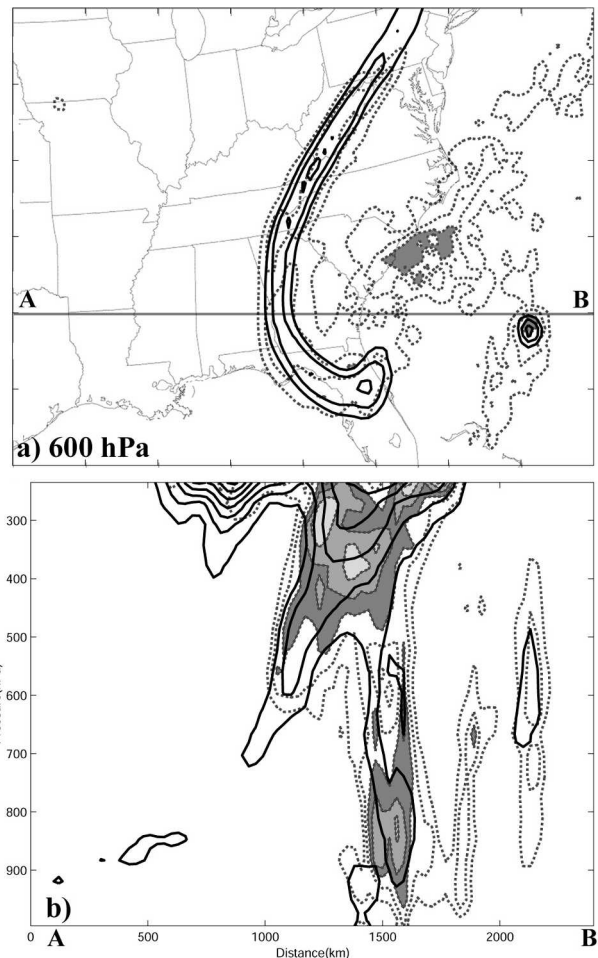


FIG. 6. The mean PV (solid, every 1.0 PVU) and its std dev (dashed, every 0.25 PVU starting from 0.5 PVU; greater than 1.0 PVU shaded) at the 24-h simulation time of EF-BGV (a) at 600 hPa and (b) along cross section AB.

with the upper-level, shortwave trough, which eventually leads to the explosive cyclogenesis, is maximized over the Appalachian Mountains and stretches to the south, collapsing into a filament as well as penetrating into the middle to lower troposphere (not shown). In the meantime, the PV variations gain coherent structure and are maximized on the edge of the mean PV filament. At the 24-h forecast time (Fig. 5c), the maximum mean PV is over southern Georgia. There are two PV filaments in the display domain at this time: the filament, which extends southward to the Gulf of Mexico, links the PV maximum to the subtropical jet and the filament, which extends northward toward the Atlantic coast, and links the PV maximum to the polar jet. Again, the largest PV spread at this level is approximately collocated with the strongest mean PV gradient associated with the shortwave trough (Fig. 5c). A secondary region of large PV spread is located above the

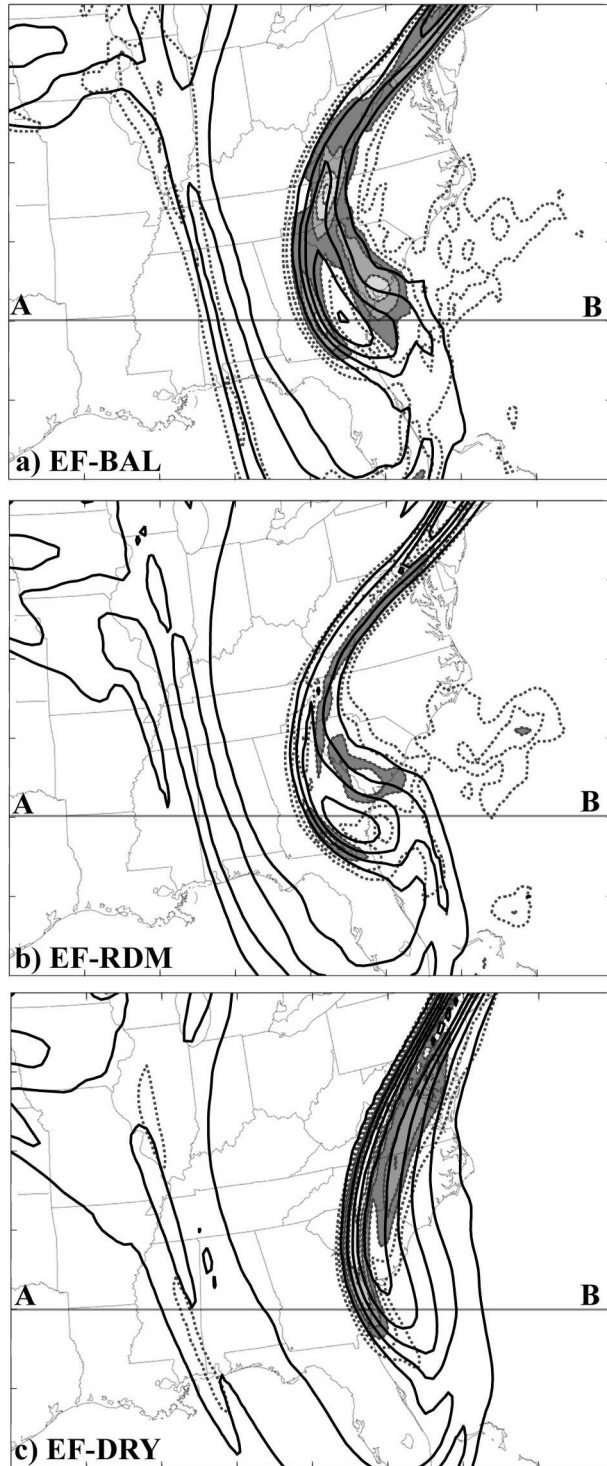


FIG. 7. Same as in Fig. 5c but for (a) EF-BAL, (b) EF-RDM, and (c) EF-DRY.

surface cyclone (Fig. 5c), where there is active moist convection. The tropopause folding associated with the upper-level shortwave trough has penetrated well below 600 hPa (Fig. 6b). Meanwhile, at the 600-hPa level,

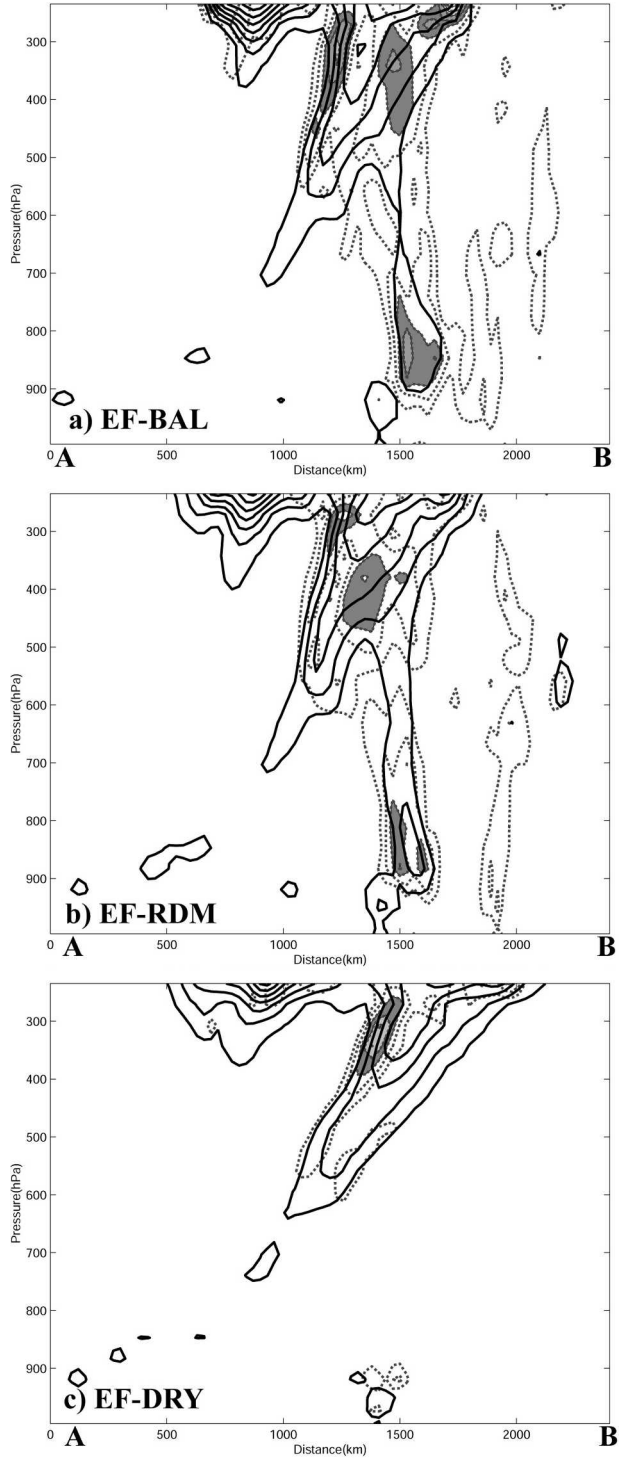


FIG. 8. Same as in Fig. 6b but for (a) EF-BAL, (b) EF-RDM, and (c) EF-DRY.

the PV spread above the convective region has a stronger maximum than that of the PV spread due directly to the intruding PV trough (Fig. 6a). The mean PV and its standard deviation in a west–east cross section are plot-

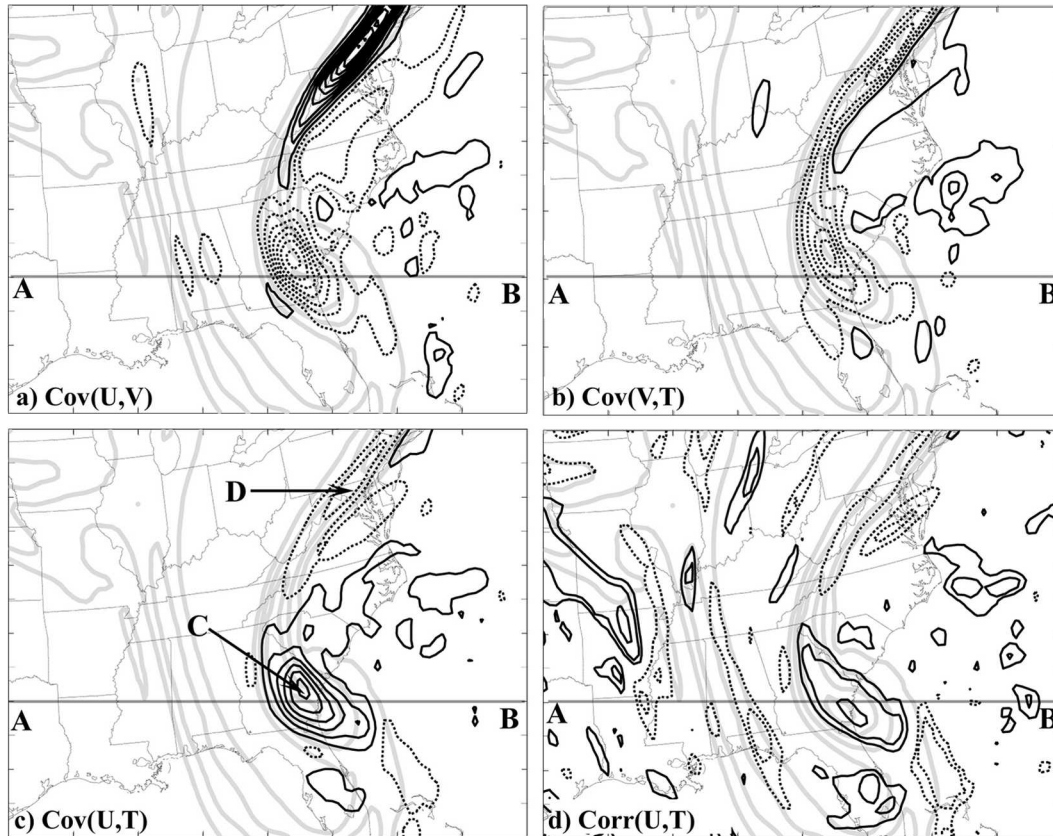


FIG. 9. The 24-h EF-BGV forecast estimated error covariance between (a)  $U$  and  $V$ , (b)  $V$  and  $T$ , and (c)  $U$  and  $T$  at 300 hPa. (d) The correlations between  $U$  and  $T$  at 300 hPa. Positive values are in solid contours and negative in dashed contour with intervals of  $10 \text{ m}^2 \text{ s}^{-2}$ ,  $2 \text{ K m s}^{-1}$ ,  $2 \text{ K m s}^{-1}$ , and  $0.2$ , respectively. Contours with correlations smaller than  $0.5$  but greater than  $-0.5$  are omitted in (d). Mean PV (gray, every  $1.0 \text{ PVU}$ ) is also plotted as a reference of the background balanced dynamics. Line AB and points C and D will be referred to in subsequent figures.

ted in Fig. 6b. Consistent with the horizontal plots, Fig. 6b shows that the upper-level, shortwave trough, along with the enhancement of lower-tropospheric diabatic PV generation (refer to ZSR02), contributes directly to the surface cyclogenesis. Also, the strongest PV variation is again seen along the PV gradient and above the region of moist convection (cf. to Fig. 5c). At the mature stage of the cyclogenesis (24–36 h), the mean upper-level PV maximum closely collocates with the surface cyclone. Consequently, the two maximum spreads, one due to the upper PV gradient and the other due to diabatic contribution, become inseparable at this time (Fig. 6b), corresponding well to the lower predictability in this region (ZSR02 and ZSR03).

The distribution of the mean and standard deviation of PV in EF-BAL and EF-RDM at 300 hPa (Figs. 7a,b) and along cross section AB (Figs. 8a,b) is qualitatively similar to that of EF-BGV (Figs. 5c and 6b), suggesting the balanced error growth dynamics is not an artifact of

ensemble initiation but rather determined by the background dynamics. For example, in both ensemble sets, the maximum PV variations collocate with the maximum PV gradient along both sides of the PV filament and a secondary region of maximum variations collocate with areas of moist processes. The magnitude of the PV variation at 300 hPa in EF-BAL is comparable to EF-BGV as well, but is slightly smaller in EF-RDM.

In EF-DRY, in which no latent heating/cooling is included in the ensemble forecast, the spread of the short-term forecast is greatly reduced. The intensity, structure, and location of the surface cyclones in all ensemble members (not shown) are very similar to the unperturbed reference simulation discussed in ZSR02 (their Fig. 8b). The maximum location and intensity differences of the primary surface cyclone among all 20 members are  $60 \text{ km}$  and  $2 \text{ hPa}$ , respectively. Smaller ensemble spread is also found in ensemble forecasts

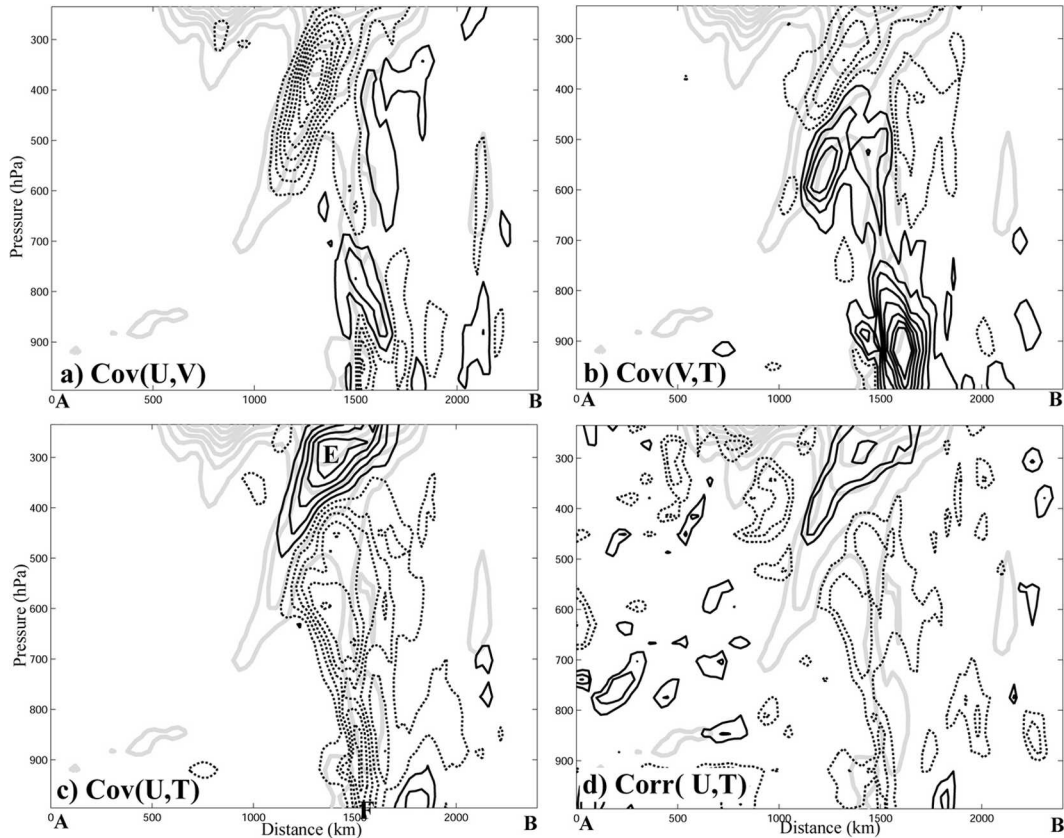


FIG. 10. Same as in Fig. 9 but along cross section AB. Points E at 300 mb and F at the surface will be referred to in Figs. 12–13.

similar to EF-DRY, but with the same balance initial perturbations as in EF-BAL (not shown). All these results are consistent with the findings from ZSR03 that moist convection strongly impacts the error growth dynamics of this event, even though the initial spreads (errors) are considerably larger in the current ensemble runs than those used by ZSR03. There are similarities in the basic features of the upper-level PV trough and the location of maximum PV variations between EF-DRY and EF-BGV (cf. Figs. 7c and 5c) at the 24-h forecast time. Nevertheless, significant differences exist between these two sets of ensemble runs as well. In EF-DRY, the upper PV trough moves too quickly to the east with less anticyclonic curvature (Fig. 7c). The PV filamentation (tropopause folding), which was directly linked to the rapid cyclogenesis in EF-BGV, barely reaches the 600-hPa level (Fig. 8c) and is no longer directly phase locked with the surface cyclone in EF-DRY. As a result, the surface cyclones in EF-DRY are all significantly weaker (10–15 hPa) than those in EF-BGV (not shown), consistent with the sensitivities between two unperturbed reference simulations found previously in ZSR02 (their Figs. 5d and 8b).

Moist processes not only modified the mean dynamics of the baroclinic system, they also changed the magnitude and distributions of the forecast uncertainty. In the upper troposphere, variations of the PV in EF-DRY are narrowly focused along the upper-level front (Figs. 7c and 8c), but they have similar magnitude to the PV variations of EF-BGV. Moreover, the significant mid-lower-tropospheric maxima above the surface cyclone and coastal front in EF-BGV (Figs. 5c and 6) are nearly absent in EF-DRY (Fig. 8c).

The evolution from small-scale uncorrelated random noise to systematic larger-scale balanced perturbations and the collocation of the maximum PV variation with local maxima along the mean PV gradient is qualitatively similar to the previous findings from ensemble forecasts with a dry quasigeostrophic model (Snyder et al. 2003; Snyder and Hamill 2003). However, examination of the PV variation suggests that caution should be taken in generalizing findings on ensemble generation or data assimilation derived from lower-dimensional dry models to more complex prediction systems simulating a realistic atmosphere in which moist dynamics have profound impacts on the error growth dynamics.

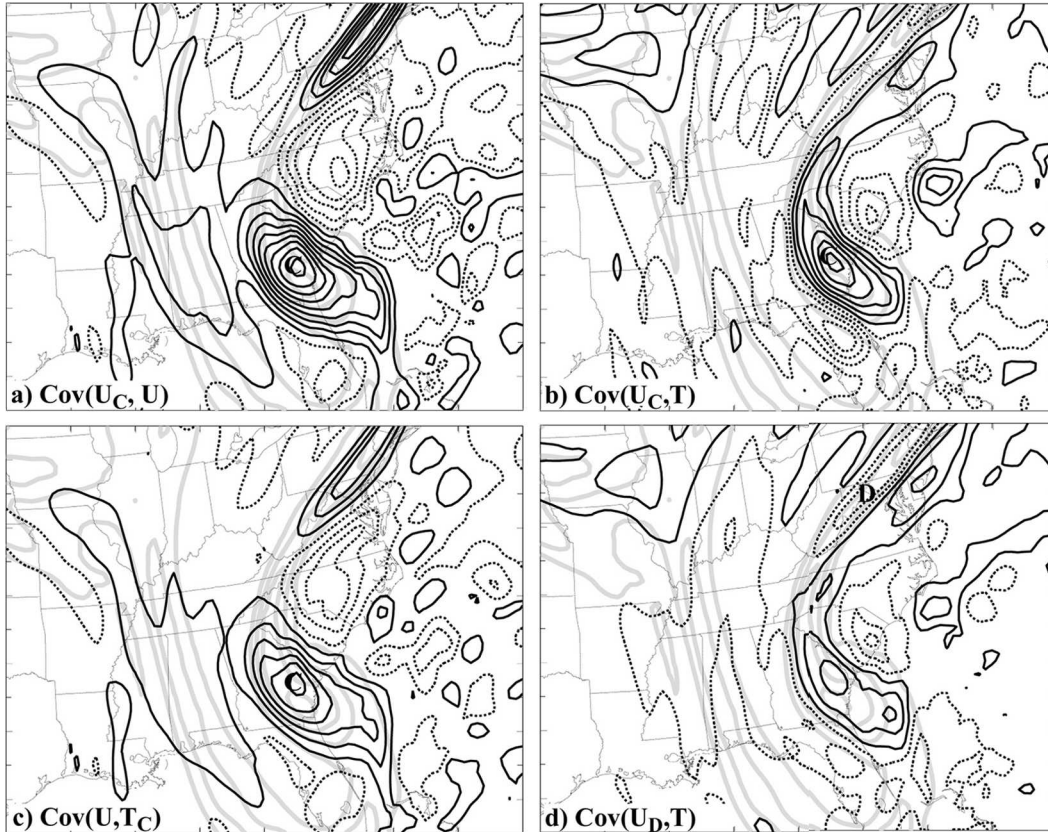


FIG. 11. The 24-h “EF-BGV” forecast estimated spatial and cross-spatial covariance between (a)  $U$  at point C and any  $U$ , (b)  $U$  at point C and any  $T$ , (c)  $T$  at point C and any  $U$ , and (d)  $U$  at point D and any  $T$ , all at 300 hPa valid at 0000 UTC 25 Jan 2000. Positive values are in solid contours and negative in dashed contours with intervals of  $10 \text{ m}^2 \text{ s}^{-2}$ ,  $2 \text{ K m s}^{-1}$ ,  $2 \text{ K m s}^{-1}$ , and  $2 \text{ K m s}^{-1}$ , respectively. The mean PV (gray, every 1.0 PVU) is also plotted as a reference of the background balanced dynamics. Points C and D are the locations with maximum and minimum cross covariance between  $U$  and  $T$  denoted in Fig. 9c.

#### 4. Error covariance

Flow-dependent error growth dynamics examined in the previous section motivate the examination of flow-dependent background error covariance, the significance of which has been pointed out by Cohn and Parrish (1991), Daley (1992), Evensen (1994), Cohn (1997), and Talagrand (1997). Special attention is given to the covariance estimated at the 24-h forecast time at which random initial perturbations will have had sufficient time to evolve into coherent structure. In practice, shorter-term ensemble forecasts and thus shorter assimilation cycles (6 or 12 h) may be used, though the covariance estimated from EF-BGV and EF-RDM may be noisier at earlier times due to the largely unbalanced nature of the initial perturbations. In addition, due to the large dimension of the error covariance matrix ( $\sim 10^{14}$ ), only a small subset of the covariance matrix will be examined.

The error covariance between any two model-state

vectors estimated with the ensemble forecasts utilized here is defined as

$$\text{Cov}\{x_{i_1 j_1 k_1} y_{i_2 j_2 k_2}\} = \frac{1}{N-1} \sum_{n=1}^N (x_{i_1 j_1 k_1 n} - \overline{x_{i_1 j_1 k_1}}) \times (y_{i_2 j_2 k_2 n} - \overline{y_{i_2 j_2 k_2}}), \quad (3)$$

where  $x_{i_1 j_1 k_1}$  and  $y_{i_2 j_2 k_2}$  represent two model-state variables located at model grid points  $(i_1, j_1, k_1)$  and  $(i_2, j_2, k_2)$ , respectively;  $n$  indexes each ensemble member;  $N$  is the total number of ensemble members ( $N = 20$ ); and the overbar denotes the mean averaged over all ensemble members. In addition to the variance of each state vector, the covariance matrix contains three typical types of covariance, named conventionally as cross covariance, spatial covariance, and cross-spatial covariance. The cross covariance is defined as the covariance between two different forecast variables at the same grid point [ $x \neq y$ ,  $(i_1, j_1, k_1) = (i_2, j_2, k_2)$ ], the spatial

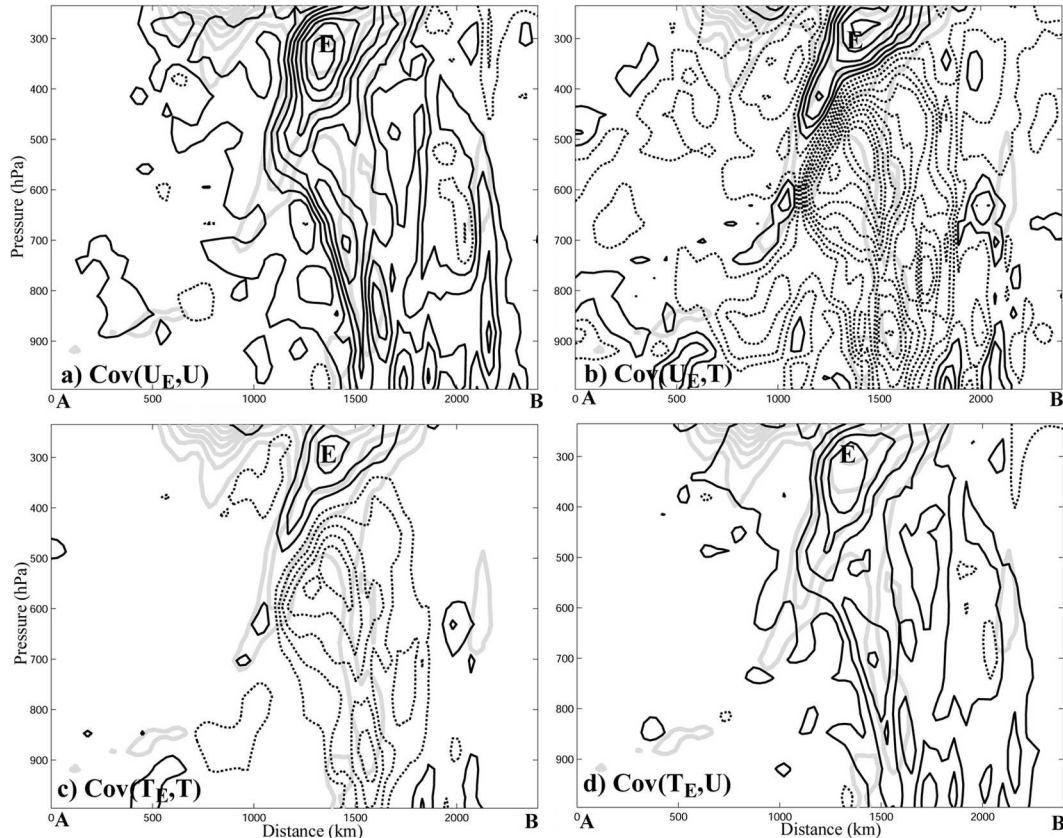


FIG. 12. Same as in Fig. 11 but the covariance of (a)  $U$  and (b)  $T$  with  $U$  at the fixed 300-hPa point E and of (c)  $T$  and (d)  $U$  with  $T$  at point E. Contour intervals for (a)–(d) are  $10 \text{ m}^2 \text{ s}^{-2}$ ,  $2 \text{ K m s}^{-1}$ ,  $0.5 \text{ K}^2$ , and  $2 \text{ K m s}^{-1}$ , respectively.

(auto) covariance is defined as the covariance between the same forecast variables at different grid points [ $x = y$ ,  $(i_1, j_1, k_1) \neq (i_2, j_2, k_2)$ ], and the cross-spatial covariance is defined as the covariance between different forecast variables at different grid points [ $x \neq y$ ,  $(i_1, j_1, k_1) \neq (i_2, j_2, k_2)$ ]. In terms of data assimilation, the cross (and cross spatial) covariance determines the amount of information propagated from one observed state variable to the other variables, while the spatial (and cross spatial) covariance determines the spread of observational information in space.

The cross covariances between  $U$  and  $V$ ,  $V$  and  $T$ , and  $U$  and  $T$  at 300 hPa at the 24-h forecast time are shown in Figs. 9a–c, respectively. Significant cross covariance is primarily found along the upper-level PV fronts over the coast and above the mean surface cyclone. The distribution of the cross covariance is collocated with the maximum mean PV or maximum PV gradient and spread (Fig. 5c), indicating its strong dependence on the background flow and the associated error growth dynamics (“error of the day”; Kalnay 2003). In the study of planetary-scale dynamics, Bran-

stator (1995) proposed to explain the synoptic eddy fluxes (essentially covariance) associated with the background general circulation by assuming random initial disturbances are assumed to evolve linearly over a short time interval on the background flow (similar to the flux-gradient theory in explaining mean turbulent flux transport; Holton 1992, chapter 5). For the present study, the meso- to small-scale deviations (errors) in the individual members may be treated as if they are turbulent eddies with respect to the background synoptic-scale cyclones, which are assumed to evolve linearly over a short time interval on the mean larger-scale flow.

Since the mean winds follow the upper-level PV trough closely, a strong positive gradient of  $V$  exists over the Carolinas and Georgia (Fig. 2d). Intuitively, if there is negative deviation of  $U$  (i.e.,  $U' < 0$ ), as is the case of member 1 over Georgia, this deviation will bring in higher  $V$  toward the west, which results in  $V' > 0$  (Figs. 2b,d). On the other hand, a positive  $U'$  over North Carolina will bring in lower  $V$  eastward ( $V' < 0$ ). In either case, the flow pattern will result in a negative covariance between  $U$  and  $V$  following the onshore

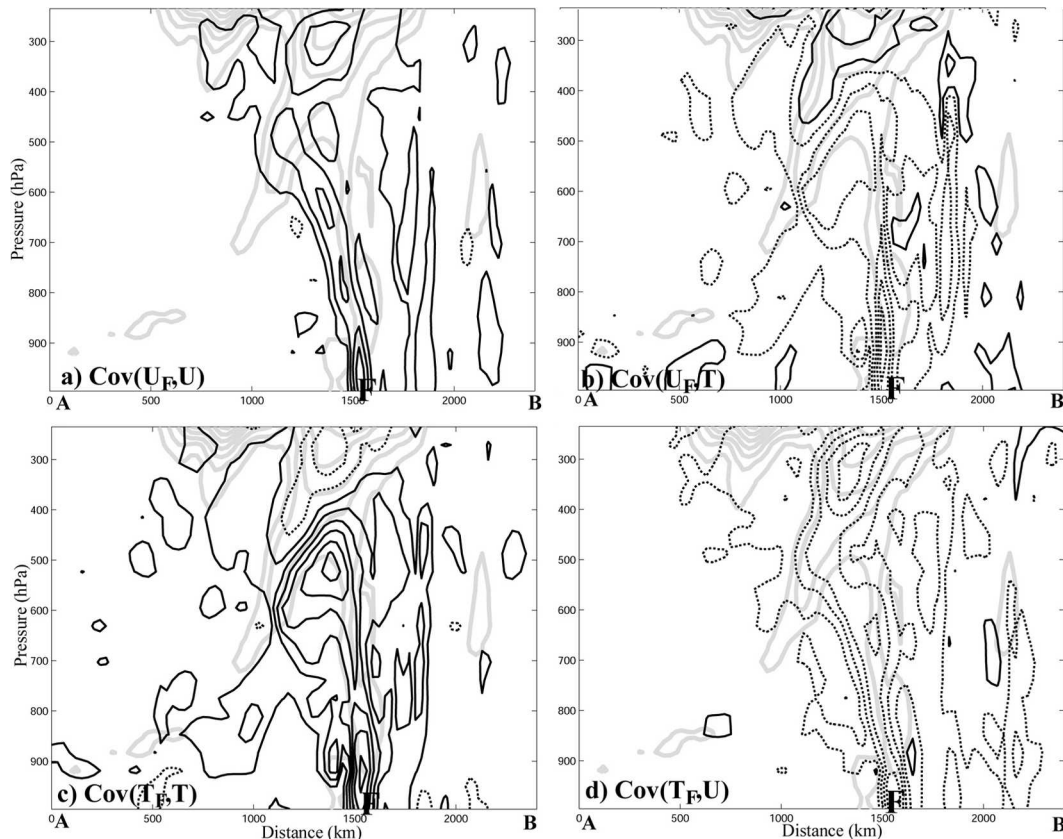


FIG. 13. Same as in Fig. 12 except for at the fixed surface point F.

flow along the Georgia and South Carolina border (Fig. 9a). Similar arguments can be made to explain the predominantly positive covariance between  $U$  and  $T$  to the south of the PV trough (Fig. 9c). However, since the flow is fully three dimensional, the gradient-transport theory based purely on the horizontal gradient cannot explain the covariance or correlations among all variables over the entire domain (Fig. 12, later). For the same reason, parameterization of the error covariance relying solely on the mean background gradient may be hard to achieve, if not impossible.

The correlation between  $U$  and  $T$  at 300 hPa is examined as well (Fig. 9d). The cross covariance is equal to the correlation between two variables multiplied by the standard deviations of both variables. Consistent with the covariance field, strong positive correlations between  $U$  and  $T$  (with maximum correlations from 0.7 to 0.9) are evident along the Georgia and South Carolina border, and are collocated with the local PV maximum as well as with the maximum variance. Negative correlations persist for the northern offshore outflow jet and inside the northern piece of the PV filament.

The cross covariance and correlation in the cross sections in Fig. 10 provide further evidence for the strong

dependence of the covariance structure on the balanced dynamics and the associated error growth at all levels. There are also interesting but intriguing vertical variations of the covariance, especially across the mean dynamic tropopause. For example, the covariance between  $U$  and  $T$  (Fig. 10c) is generally positive above the tropopause (point E denotes the maximum in the middle of the shortwave trough at 300 hPa), but is predominantly negative in the mid- to lower atmosphere with a minimum above the surface frontal boundary (point F denotes the minimum at the surface). Note also that there are significant correlations between  $U$  and  $T$  in other parts of the domain where covariance is small (Figs. 9d and 10d). These strong correlations are consistent with the mean balanced dynamics in those regions. In terms of data assimilation, regions with large correlation but small covariance are only of marginal importance because of the small background uncertainties in those regions.

Next, we examine the structure of spatial and cross-spatial covariance which determines how to spread the observational information spatially to the same variable or to different variables when observations are assimilated. The maximum and minimum covariance between

$U$  and  $T$  (points C and D in Fig. 9c), respectively, are selected as the two hypothetical observational sites. The spatial (auto) covariance between  $U$  at point C and all other points at the 300-hPa level is plotted in Fig. 11a. It is obvious that the covariance is not isotropic. The structure of the autocovariance is also evidently constrained by the background mean (flow dependent) dynamics. Similar conclusions can be drawn from the flow-dependent cross-spatial covariance between  $U$  at points C and D with  $T$  (Figs. 11b,d) and between  $T$  at point C with  $U$  at other points (Fig. 11c). Significant covariances exist between both  $U$  and  $T$  at points C with different variables at locations all across the display domain, indicating the radius of influence of observations at point C is well above 1000 km. Moreover, information from observations of  $U$  or  $T$  at 300 hPa (point E of Fig. 10c) can influence state variables at different vertical levels including the surface through the vertical covariance structure revealed in Fig. 12. Observation information at the surface (point F in Fig. 13c) can also be spread to the upper troposphere through the covariance structure displayed in Fig. 13. These covariance structures demonstrate the potential for an ensemble-based data assimilation system to effectively cope with the apparent inhomogeneity of observations at different layers and at different locations given the relative abundance of surface observations compared to the sounding network. The value of surface observations was demonstrated recently for the convective scales by Zhang et al. (2004) and in global EnKF experiments by Whitaker et al. (2004).

The representativeness of the error covariance structure discussed above is examined through the covariance structure estimated from the other two independent sets of ensemble forecasts (EF-BAL and EF-RDM). To a first-order approximation, the structure of the error covariance estimated from these two independent ensemble forecasts (Figs. 14a,b and 15a,b) agrees well with that estimated from EF-BGV discussed above (Figs. 9c and 10c). The magnitude of the covariance also maximizes near the PV front zones and above the surface cyclogenesis. Even smaller differences in the structure and magnitude of the error covariance are found in ensemble forecasts the same as EF-BAL but with a larger (doubled) ensemble size (Fig. 16 versus Figs. 14a and 15a), consistent with Houtekamer and Mitchell (1998, their Fig. 6). It is worth noting that the covariance fields estimated from the 40-member ensemble (Fig. 16) are noticeably smoother than those from the 20-member ensemble (Figs. 14a and 15a).

Due to the complexity of model errors, especially in the representation of moist physics, the sensitivity of the error covariance to the imperfectness of the fore-

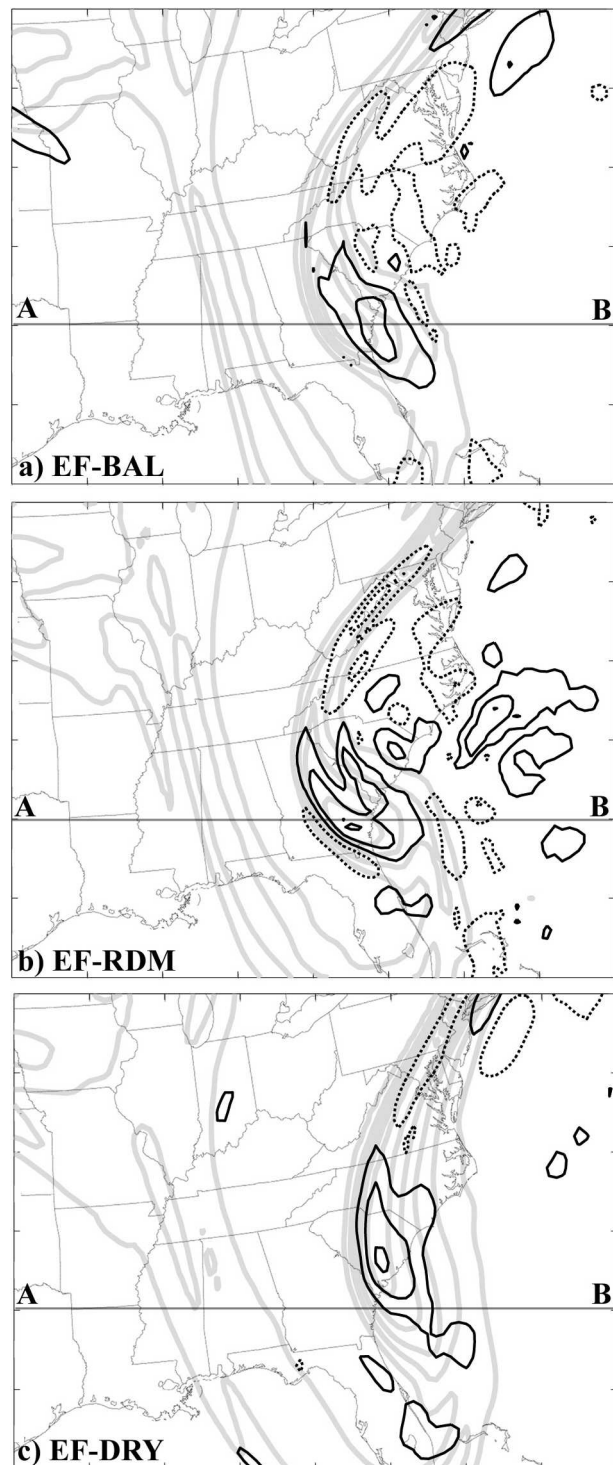


FIG. 14. Same as in Fig. 9c but for (a) EF-BAL, (b) EF-RDM, and (c) EF-DRY. Contour intervals in (a)–(c) are 2, 2, and 1  $\text{K m s}^{-1}$ , respectively.

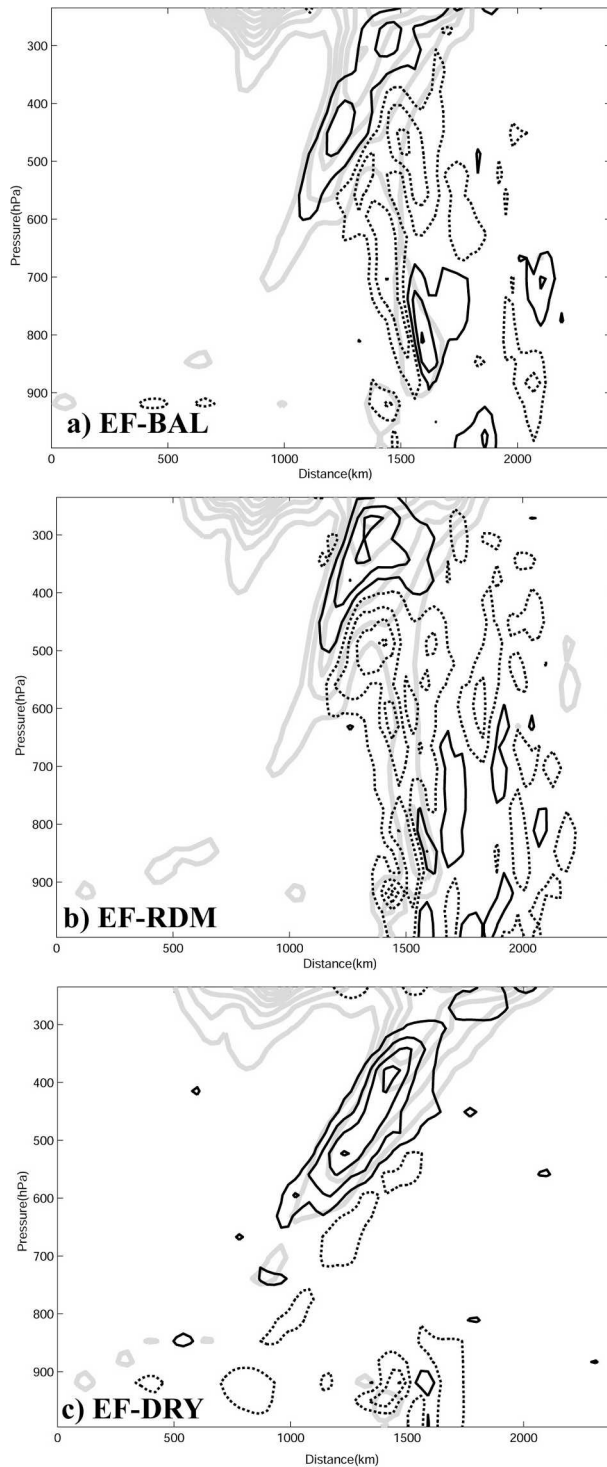


FIG. 15. Same as in Fig. 10c but for (a) EF-BAL, (b) EF-RDM, and (c) EF-DRY. Contour intervals in (a)–(c) are 2, 2, and 1  $\text{K m s}^{-1}$ , respectively.

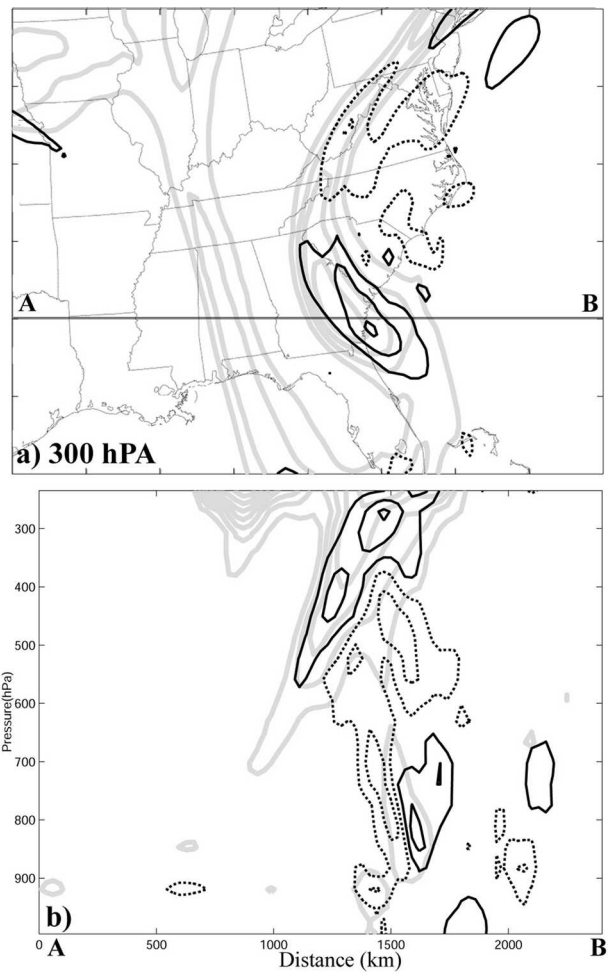


FIG. 16. (a) Same as in Fig. 14a except for using 40 ensemble members. (b) Same as in Fig. 15a except for using 40 ensemble members.

cast model is beyond the scope of the current paper [refer to Mitchell et al. (2002) for a discussion of this subject in the context of the EnKF]. There are large differences, especially in magnitude, between the error covariance estimated from EF-BGV and EF-DRY with and without the diabatic heating feedback (cf. Figs. 10c, 11c, 14c, and 15c), which is consistent with different error growth dynamics associated with a different mean estimate (Figs. 7c and 8c). Nevertheless, there are strong similarities between covariance structures from EF-BGV and EF-DRY, suggesting valuable information can be extracted from the forecast error covariance estimate associated with a biased mean forecast with an imperfect model.

The flow-dependent, nonstationary, and anisotropic nature of the background error covariance is further seen in the difference of sign and magnitude, structure, and dynamics of the covariance estimated from the

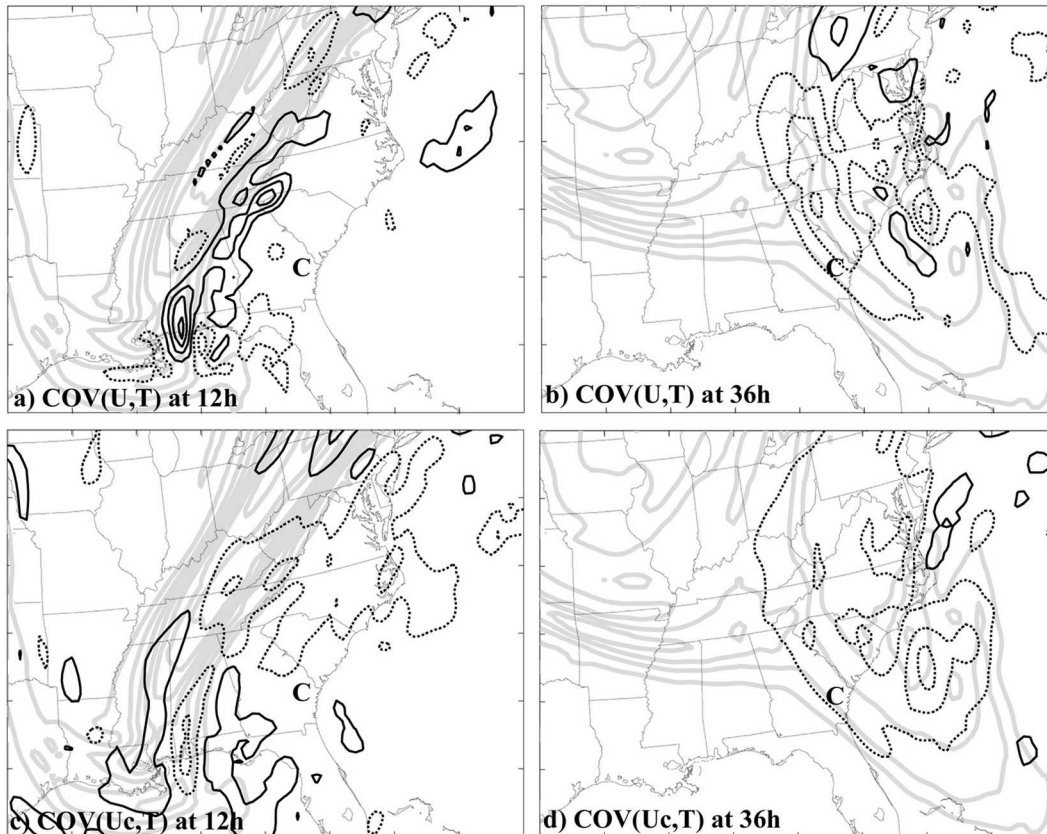


FIG. 17. (a), (b) Same as in Fig. 9c but for cross covariance between  $U$  and  $T$  valid at the (a) 12- and (b) 36-h forecast time. (c), (d) Same as in Fig. 11b but for cross-spatial covariance between  $U$  at point C and any  $T$  valid at (c) 12 and (d) 36 h.

same set of ensemble forecast but verified at different times. For example, the 300-hPa covariances between  $U$  and  $T$  at 12 and 36 h (Figs. 17a,b) are completely different from the covariance estimated at 24 h (Fig. 9c). The covariance structure is also consistent with background mean dynamics and the associated error growth at the respective times (Figs. 5b,c,d). The covariance between  $U$  at point C and  $T$  at any 300-hPa point valid at 1200 UTC 24 January and 1200 UTC 25 January (Figs. 17c,d) is much smaller than (and is often opposite in sign to) that valid at 0000 UTC 25 January (Fig. 11b) in addition to the larger difference in structure at different times.

## 5. Summary and conclusions

In this study, short-term ensemble forecasts generated with different sets of initial perturbations were used to examine the dynamics and structure of meso-scale error covariance of the 24–25 January 2000 surprise snowstorm that occurred along the East Coast of the United States, complementary to our previous pre-

dictability studies of the same event (ZSR02; ZSR03). In the ensemble forecast initiated with rescaled, breeding random perturbations (EF-BGV), initial errors grow from smaller-scale, largely unbalanced uncorrelated perturbations to larger-scale, quasi-balanced disturbances with coherent structures within 12–24 h. Comparable ensemble spread is found in ensemble forecasts initialized with balanced random perturbations (EF-BAL) or with “gridpoint” random perturbations (EF-RDM). In all ensemble forecasts, the error growth is maximized in the vicinity of the strongest mean PV gradient and/or over the area of active moist convection, consistent with the lower predictability in these regions (ZSR02; ZSR03). The scale change of growing error and its dependence on the background dynamics are also consistent with findings in previous studies (Farrell 1990; Buizza 1994; Barkmeijer et al. 1998; ZSR03; Tribbia and Baumhefner 2004).

Consequently, the initially largely uncorrelated, mostly random perturbations evolve into strong coherent structures with spatial correlation not only among the same variable (autocovariance) but also between

different forecast variables (cross covariance), especially over the region of strong cyclogenesis and along the upper-level front. The error covariance is highly anisotropic. Dramatic differences in magnitude, structure, and sign are found between covariance estimated from the same set of ensemble forecasts but valid at different times. The structure of the mesoscale error covariance is ultimately determined by the underlying governing dynamics and its associated error growth. The spatial and cross covariance estimated from the short-term ensemble forecast have the potential to spread observational information nonuniformly to both observed and unobserved variables at different vertical layers (e.g., from the upper troposphere to the surface and vice versa) with a horizontal radius of influence potentially greater than 1000 km. The flow-dependent nature of the error growth dynamics and covariance structure further demonstrates the necessity to use anisotropic and flow-dependent representations of background error covariance for meso-/regional data assimilation (e.g., Cohn and Parrish 1991). In addition, the flow-dependent covariance information derived from the ensemble forecast can be used to determine where the optimum observations (i.e., “targeted observation”) should be taken by maximizing the Kalman gain (e.g., Bishop et al. 2001; Hamill and Snyder 2002).

The dynamics and structure of the error covariance estimated from ensemble forecasts generated with different sets of initial perturbations are qualitatively similar but differs in details. Sensitivity of the error covariance to model error is not examined in the current work but similarities between estimates from ensemble forecasts with and without diabatic feedback suggest that even a biased ensemble forecast from an imperfect model still contains useful information of the forecast error covariance.

The significance and effectiveness of the error covariance estimated from the above ensemble forecasts have been tested in an EnKF data assimilation system based on MM5 for this event. Results from these EnKF experiments will be reported elsewhere.

*Acknowledgments.* The author is very grateful to the anonymous reviewers for their constructive comments for improving the manuscript. Thanks are also due to Chris Snyder, Rich Rotunno, Dale Barker, Craig Bishop, Jun Du, Tom Hamill, John Nielsen-Gammon, Wei Huang, Courtney Schumacher, Altug Aksoy, and Ellie Meng for their comments on this subject. This research is supported by NSF Grant ATM 0205599 and by the Office of Navy Research under the Young Investigator Program (Award N000140410471).

## REFERENCES

- Barker, D. M., W. Huang, Y.-R. Guo, and A.J. Bourgeois, 2003: A three-dimensional variational (3DVAR) data assimilation system for use with MM5. NCAR Tech. Note NCAR/TN-453+STR, 68 pp.
- , —, —, —, and Q. N. Xiao, 2004: A three-dimensional variational data assimilation system for MM5: Implementation and initial results. *Mon. Wea. Rev.*, **132**, 897–914.
- Barkmeijer, J., M. van Gijzen, and F. Bouttier, 1998: Singular vectors and estimates of the analysis-error covariance metric. *Quart. J. Roy. Meteor. Soc.*, **124**, 1695–1713.
- Benjamin, S. O., and N. L. Seaman, 1985: A simple scheme for objective analysis in curved flow. *Mon. Wea. Rev.*, **113**, 1184–1198.
- Bishop, C. H., B. J. Etherton, and S. J. Majumdar, 2001: Adaptive sampling with the ensemble transform Kalman filter. Part I: Theoretical aspects. *Mon. Wea. Rev.*, **129**, 420–436.
- Branstator, G., 1995: Organization of storm track anomalies by recurring low-frequency circulation anomalies. *J. Atmos. Sci.*, **52**, 207–226.
- Buizza, R., 1994: Sensitivity of optimal unstable structures. *Quart. J. Roy. Meteor. Soc.*, **120**, 429–451.
- , and P. Chessa, 2002: Prediction of the U.S. storm of 24–26 January 2000 with the ECMWF ensemble prediction system. *Mon. Wea. Rev.*, **130**, 1531–1551.
- Cohn, S. E., 1997: An introduction to estimation theory. *J. Meteor. Soc. Japan*, **75**, 257–288.
- , and D. F. Parrish, 1991: The behavior of forecast error covariances for a Kalman filter in two dimensions. *Mon. Wea. Rev.*, **119**, 1757–1785.
- Daley, R., 1992: Forecast error statistics for homogeneous and inhomogeneous observation networks. *Mon. Wea. Rev.*, **120**, 627–643.
- Dowell, D. C., F. Zhang, L. J. Wicker, C. Snyder, and N. A. Crook, 2004: Wind and temperature retrievals in the 17 May 1981 Arcadia, Oklahoma, supercell: Ensemble Kalman filter experiments. *Mon. Wea. Rev.*, **132**, 1982–2005.
- Du, J., S. L. Mullen, and F. Sanders, 1997: Short-range ensemble forecasting of quantitative precipitation. *Mon. Wea. Rev.*, **125**, 2427–2459.
- Dudhia, J., 1993: A nonhydrostatic version of the Penn State/NCAR Mesoscale Model: Validation tests and simulation of an Atlantic cyclone and cold front. *Mon. Wea. Rev.*, **121**, 1493–1513.
- Errico, R., and D. Baumhefner, 1987: Predictability experiments using a high-resolution limited area model. *Mon. Wea. Rev.*, **115**, 488–504.
- Evensen, G., 1994: Sequential data assimilation with a nonlinear quasi-geostrophic model using Monte Carlo methods to forecast error statistics. *J. Geophys. Res.*, **99** (C5), 10 143–10 162.
- Farrell, B. F., 1990: Small error dynamics and the predictability of atmospheric flows. *J. Atmos. Sci.*, **47**, 2409–2416.
- Hamill, T. M., 2005: Ensemble-based atmospheric data assimilation. *Predictability of Weather and Climate*, R. Hagedorn and T.N. Palmer, Eds., Cambridge University Press, in press.
- , and C. Snyder, 2000: A hybrid ensemble Kalman filter/3D-variational analysis scheme. *Mon. Wea. Rev.*, **128**, 2905–2919.
- , and —, 2002: Using improved background-error covariances from an ensemble Kalman filter for adaptive observations. *Mon. Wea. Rev.*, **130**, 1552–1572.

- Holton, J. R., 1992: *An Introduction to Dynamic Meteorology*. Academic Press, 511 pp.
- Houtekamer, P. L., and H. L. Mitchell, 1998: Data assimilation using an ensemble Kalman filter technique. *Mon. Wea. Rev.*, **126**, 796–811.
- , —, G. Pellerin, M. Buehner, M. Charron, L. Spacek, and B. Hansen, 2005: Atmospheric data assimilation with an ensemble Kalman filter: Results with real observations. *Mon. Wea. Rev.*, **133**, 604–620.
- Jang, K.-I., X. Zou, M. S. F. V. De Pondeca, M. Shapiro, C. Davis, and A. Krueger, 2003: Incorporating TOMS ozone measurements into the prediction of the Washington, D.C., winter storm during 24–25 January 2000. *J. Appl. Meteor.*, **42**, 797–812.
- Kalnay, E., 2003: *Atmospheric Modeling, Data Assimilation and Predictability*. Cambridge University Press, 341 pp.
- Keppenne, C. L., 2000: Data assimilation into a primitive-equation model with a parallel ensemble Kalman filter. *Mon. Wea. Rev.*, **128**, 1971–1981.
- , and M. M. Rienecker, 2002: Initial testing of a massively parallel ensemble Kalman filter with the Poseidon isopycnal ocean general circulation model. *Mon. Wea. Rev.*, **130**, 2951–2965.
- Langland, R. H., M. A. Shapiro, and R. Gelaro, 2002: Initial condition sensitivity and error growth in the forecast of the 25 January 2000 East Coast snowstorm. *Mon. Wea. Rev.*, **130**, 957–974.
- Lorenz, E. N., 1969: The predictability of a flow which possesses many scales of motion. *Tellus*, **21**, 289–307.
- Mesinger, F., 1998: Comparison of Quantitative Precipitation Forecasts by the 48- and by the 29-km Eta Model: An update and possible implications. Preprints, *16th Conf. on Weather Analysis and Forecasting/Symp. on Research Foci of the U.S. Weather Research Program*, Phoenix, AZ, Amer. Meteor. Soc., J106–J107.
- Mitchell, H. L., P. L. Houtekamer, and G. Pellerin, 2002: Ensemble size, balance and model-error representation in an ensemble Kalman filter. *Mon. Wea. Rev.*, **130**, 2791–2808.
- Molteni, F., R. Buizza, T. N. Palmer, and T. Petroliaigis, 1996: The ECMWF ensemble prediction system: Methodology and validation. *Quart. J. Roy. Meteor. Soc.*, **122**, 73–120.
- Mullen, S. L., J. Du, and F. Sanders, 1999: The dependence of ensemble dispersion on analysis–forecast systems: Implications to short-range ensemble forecasting of precipitation. *Mon. Wea. Rev.*, **127**, 1674–1686.
- Snyder, C., and T. M. Hamill, 2003: Leading Lyapunov vectors of a turbulent baroclinic jet in a quasigeostrophic model. *J. Atmos. Sci.*, **60**, 683–688.
- , and F. Zhang, 2003: Assimilation of simulated radar observations with an ensemble Kalman filter. *Mon. Wea. Rev.*, **131**, 1663–1677.
- , T. M. Hamill, and S. B. Trier, 2003: Linear evolution of error covariances in a quasigeostrophic model. *Mon. Wea. Rev.*, **131**, 189–205.
- Stensrud, D. J., H. E. Brooks, J. Du, M. S. Tracton, and E. Rogers, 1999: Using ensembles for short-range forecasting. *Mon. Wea. Rev.*, **127**, 433–446.
- Talagrand, O., 1997: Assimilation of observations, an introduction. *J. Meteor. Soc. Japan*, **75**, 191–209.
- Toth, Z., and E. Kalnay, 1993: Ensemble forecasting at NMC: The generation of perturbations. *Bull. Amer. Meteor. Soc.*, **74**, 2317–2330.
- , and —, 1997: Ensemble forecasting at NCEP and the breeding method. *Mon. Wea. Rev.*, **125**, 3297–3319.
- Tracton, M. S., and E. Kalnay, 1993: Operational ensemble prediction at the National Meteorological Center: Practical aspects. *Wea. Forecasting*, **8**, 379–400.
- , and J. Du, 2001: Application of the NCEP/EMC short-range ensemble forecast system (SREF) to predicting extreme precipitation events. Preprints, *Symp. on Precipitation Extremes: Prediction, Impacts, and Responses*, Albuquerque, NM, Amer. Meteor. Soc., 64–65.
- Tribbia, J. J., and D. P. Baumhefner, 2004: Scale interactions and atmospheric predictability: An updated perspective. *Mon. Wea. Rev.*, **132**, 703–713.
- Vukicevic, T., and R. M. Errico, 1990: The influence of artificial and physical factors upon predictability estimates using a complex limit-area model. *Mon. Wea. Rev.*, **118**, 1460–1482.
- Wandishin, M. S., S. L. Mullen, D. J. Stensrud, and H. E. Brooks, 2001: Evaluation of a short-range multimodel ensemble system. *Mon. Wea. Rev.*, **129**, 729–747.
- Whitaker, J. S., G. P. Compo, X. Wei, and T. M. Hamill, 2004: Reanalysis without radiosondes using ensemble data assimilation. *Mon. Wea. Rev.*, **132**, 1190–1200.
- Zhang, F., C. Snyder, and R. Rotunno, 2002: Mesoscale predictability of the “surprise” snowstorm of 24–25 January 2000. *Mon. Wea. Rev.*, **130**, 1617–1632.
- , —, and —, 2003: Effects of moist convection on mesoscale predictability. *J. Atmos. Sci.*, **60**, 1173–1185.
- , —, and J. Sun, 2004: Impacts of initial estimate and observation availability on convective-scale data assimilation with an ensemble Kalman filter. *Mon. Wea. Rev.*, **132**, 1238–1253.
- Zhang, S., and J. L. Anderson, 2003: Impact of spatially and temporally varying estimates of error covariance on assimilation in a simple atmospheric model. *Tellus*, **55A**, 126–147.
- Zupanski, M., D. Zupanski, D. F. Parrish, E. Rogers, and G. DiMego, 2002: Four-dimensional variational data assimilation for the blizzard of 2000. *Mon. Wea. Rev.*, **130**, 1967–1988.